2025, 10(4)

e-ISSN: 2468-4376

https://www.jisem-journal.com/

Research Article

Performance Enhancement of HVDC-VSC Using FFNN-Based PI Control Under Hybrid Renewable Integration

Cherif Kellal^{1,2}, Mazouz Lakhdar², Belkheir Abdesselam³, Ali Teta¹, Matilde Pietrafesa⁴

¹ Laboratory of Applied automation and Industrial Diagnosis (LAADI), Faculty of Science and Technology, University of Djelfa, Algeria

² Renewable Energy Systems Applications Laboratory (LASER), Faculty of Science and Technology, University of Djelfa, Algeria

³ dept electrical engineering LREA Laboratory, University of Medea, Algeria
 ⁴ Department of Civil, Energetic, Environmental and Material Engineering (DICEAM), Mediterranea
 University of Reggio Calabria, Via Zehender, Loc. Feo Di Vito, 89122 Reggio Calabria, Italy
 Email: c..kellal@univ-djelfa.dz

ARTICLE INFO

ABSTRACT

Received: 30 April 2025 Revised: 19 Sept 2025 Accepted: 18 Oct 2025 This study introduces an advanced utilization of artificial neural networks (ANNs) in the feed-forward control of high-voltage direct current voltage source converters (HVDC-VSC) connected to hybrid renewable energy systems (HRES). The inherent nonlinear characteristics of renewable sources, combined with the fast-switching dynamics of power electronic converters, create significant challenges for conventional controllers in ensuring stable grid operation and efficient energy transfer. To overcome these limitations, a feed-forward neural network (FFNN)-based scheme is developed to improve DC-link voltage regulation, optimize the coordination of active and reactive power, and enhance overall system stability. The proposed FFNN is trained offline with extensive datasets that reflect diverse operating scenarios, enabling it to capture the complex relationships among renewable generation, grid variations, and converter control requirements. By predicting control actions in advance, the method reduces dependence on traditional feedback loops, thereby achieving faster transient response and greater resilience to disturbances. Simulation outcomes confirm that the FFNN controller surpasses the conventional proportional-integral (PI) approach in terms of reduced settling time, minimized steady-state error, and improved power quality, which makes it a feasible solution for modern grid applications.

Keywords: HVDC-VSC; ANN; HRES; FFNN; P&O method.

INTRODUCTION

The pressing need to curb climate change while meeting the rising global energy demand has accelerated the large-scale integration of renewable energy resources (RES), particularly wind and solar photovoltaic (PV) technologies. Nevertheless, the intermittent and unpredictable nature of these sources introduces considerable difficulties for stable grid operation, frequently causing voltage fluctuations, power imbalances, and reduced system dependability [1,2]. To address these challenges, hybrid renewable energy systems (HRES) which combine diverse RES with energy storage technologies (ESS) have been developed as a promising approach to ensure more reliable, controllable, and sustainable power generation [3].

Concurrently, HVDC transmission, especially with voltage source converters (VSCs), has emerged as a key technology due to its capability to transmit substantial power capacity across extended distances,

2025, 10(4)

e-ISSN: 2468-4376

https://www.jisem-journal.com/

Research Article

link asynchronous AC systems, and enable precise regulation of reactive and active power flows [4,5]. Coupling HRES with HVDC-VSC links provides an efficient means of transferring renewable energy from remote sources (such as offshore wind installations) while enhancing grid stability through advanced power coordination and control functionalities [6].

Despite these advancements, the effective control of such complex systems remains a critical area of research. Traditional linear control techniques, such as proportional-integral (PI) controllers, often struggle to adequately address the highly non-linear dynamics, varying operating conditions, and frequent disturbances inherent in HRES-HVDC-VSC interconnected systems [7]. These limitations highlight the need to explore more advanced and adaptive control methodologies.

ANNs, inspired by the biological brain, have the capability to learn complex nonlinear relationships from data, recognize patterns, and adapt [8,9]. These characteristics make ANNs a powerful tool for developing advanced control schemes in dynamic and uncertain environments. ANNs have been extensively explored for various power system applications. Among the different ANN architectures, the FFNN is the most widely implemented due to its structural simplicity and effectiveness in both control and regression tasks. Nevertheless, their application in feed-forward control of HVDC-VSC systems directly integrated with HRES for comprehensive system-level optimization remains a nascent yet promising field. This introduction lays the foundation for exploring how an ANN-based feed-forward control strategy can effectively manage the intricate interactions within such systems, aiming to improve DC-link voltage regulation, optimize power transfer, and enhance overall grid integration performance [10].

SYSTEM STRUCTURE

Figure 1 illustrates the configuration of an HRES that integrates PV and wind power sources through a common DC-link. The generated power is conditioned using boost converters and regulated through maximum power extraction based on the perturb and observe (P&O) method. The system is interfaced with the utility grid via a voltage source inverter (VSI), an RL filter, and a transformer, with an additional step-up transformer included to satisfy high-voltage transmission requirements. Furthermore, the overall system is connected to an HVDC-VSC transmission network, consisting of a rectifier at the sending terminal and an inverter at the receiving terminal, interconnected by DC transmission cables. This arrangement enables efficient long-distance power transfer to the receiving grid.

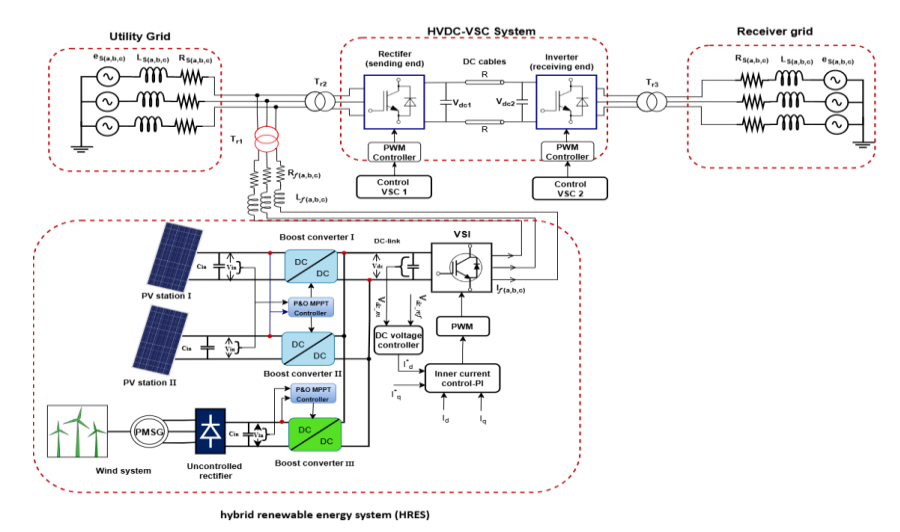


Figure 1: The overall schematic of the proposed system.

2025, 10(4)

e-ISSN: 2468-4376

https://www.jisem-journal.com/

Research Article

SYSTEM MODELING

A. MODELING A WIND ENERGY CONVERSION SYSTEM (WECS)

In the domain of WECS, several topologies exist depending on the generator type employed. In this study, a wind turbine equipped with a permanent magnet synchronous generator (PMSG), coupled with an uncontrolled rectifier followed by a DC–DC boost converter, was selected owing to its distinct advantages. These include the inherent self-excitation capability of the PMSG, the ability to regulate output voltage to meet inverter requirements, the simplicity of the control scheme, and the relatively low operational and implementation costs [11].

Modeling of a wind turbine

Mathematically, the mechanical output power P_m derived from a wind turbine is represented as:

$$P_m = \frac{1}{2}\rho \cdot \pi \cdot R^2 \cdot v_w^3 \cdot C_p(\lambda, \beta) \tag{1}$$

where $C_p(\lambda, \beta)$ represents the aerodynamic power coefficient, β refers to the blade pitch angle, and λ denotes the tip speed ratio. Additionally, v_w refers to the wind speed at the rotor, R is the rotor radius, and ρ represents the air density. Mathematically, the tip speed ratio is expressed as:

$$\lambda = \frac{R \cdot \omega_r}{v_w} \tag{2}$$

where ω_r is the rotor velocity, the power extraction efficiency of a wind turbine is described by modeling $C_p(\lambda, \beta)$ and is given as:

$$C_p(\lambda, \beta) = 0.5176 \cdot \beta \cdot \left(116 \times \frac{1}{\lambda_i} - 0.4\beta - 5\right) e^{\frac{-21}{\lambda_i}} + (0.0068 \cdot \lambda)$$
 (3)

where λ_i is specified using the following equation:

$$\frac{1}{\lambda_i} = -\frac{0.035}{1+\beta^3} + \frac{1}{(\lambda + 0.08\beta)} \tag{4}$$

The mechanical torque T_m can be calculated using the following expression:

$$T_m = \frac{P_m}{\omega_m} = \frac{1/2\rho \cdot \pi \cdot R^2 \cdot v_W^3 \cdot C_p(\lambda, \beta)}{\omega_m} \tag{5}$$

Equation 3 indicates that for a fixed pitch angle β , there is an optimal rotational speed that maximizes energy production per wind speed. Figure 2 illustrates the performance characteristics of turbine under varying wind speeds with the pitch angle set to zero.

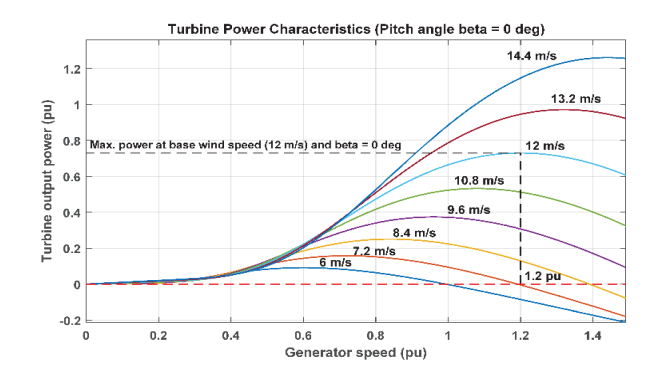


Figure 2: Power output characteristics of wind turbine.

2025, 10(4)

e-ISSN: 2468-4376

https://www.jisem-journal.com/

Research Article

Figure 2 highlights the relationship between turbine power output and rotational speed, demonstrating the process of optimizing power extraction from varying wind conditions to achieve maximum efficiency. The wind turbine operates using a PMSG. Notably, the power coefficient (C_p) reaches its peak when the blade pitch angle is set to zero. Initially, the turbine produces mechanical torque per unit, which is then converted into effective torque by scaling it with the base torque. This resultant torque is ultimately applied to the shaft of the PMSG. The maximum power output is achieved when the wind speed reaches its base value of 12 m/s, corresponding to the generator's nominal speed of 1.2 per unit [12]

Modeling of PMSG

The stator voltage equations for a PMSG are written in a synchronous d-q reference frame as below:

$$\begin{cases} V_d = R_s i_d + L_d \frac{di_d}{dt} - \omega_e L_q i_q \\ V_q = R_s i_q + L_q \frac{di_q}{dt} + \omega_e (L_d i_d + \lambda_m) \end{cases}$$
 (6)

where R_s is the stator winding resistance (Ω), i_d and i_q represent the stator currents, $L_d = L_q$ refers to the stator inductances (H), and λ_m denotes the permanent magnet flux linkage (Wb).

The electrical angular velocity of the rotor ω_e is given as:

$$\omega_e = p \cdot \omega_m \tag{7}$$

where ω_m refers to the mechanical angular velocity of the rotor, while p is the number of pole pairs in the machine.

The mechanical dynamics of the WECS are described by the following equation:

$$\frac{d\omega_m}{dt} = \frac{1}{I} \cdot (T_m - B \cdot \omega_m - T_e) \tag{8}$$

The electromagnetic torque T_e generated by PMSG can be represented as follows:

$$T_e = \frac{3}{2}p\lambda_m i_q \tag{9}$$

where J refers to the moment of total inertia of the rotor ($kg.m^2$) (in case there is no gearbox), B (N·m·s/rad) is the damping coefficient, which accounts for the rotational losses in the system.

B. MODELING OF A PV SYSTEM

The PV cell can be modeled using the equivalent circuit of a single diode [13], as shown in Figure 3.

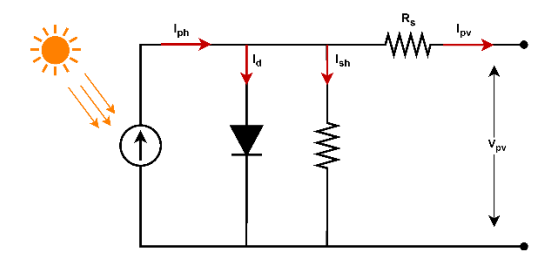


Figure 3: Equivalent circuit model of a PV cell.

2025, 10(4)

e-ISSN: 2468-4376

https://www.jisem-journal.com/

Research Article

The output current of a PV cell is described by the following expression:

$$I_{pv} = I_{ph} - I_d - I_{sh} (10)$$

The current passing through the shunt resistor
$$I_{sh}$$
 is given by the expression:
$$I_{sh} = \frac{V_{pv} + R_s I}{R_{sh}}$$
 (11)

The current of shockley diode I_d is given by the expression:

$$I_d = I_0 \left[\exp \left[\frac{q(V_{pv} + R_S I)}{AkT} \right] - 1 \right] \tag{12}$$

where I_0 is diode saturation current (A), R_s and R_{sh} represent the series and shunt resistances (Ω), respectively. T is cell temperature (K), q is the charge of an electron, V_{pv} is voltage across the cell, A is ideality factor of the diode, k is Boltzmann constant.

The expression for the photocurrent I_{ph} generated from light is as follows:

$$I_{ph} = \frac{G}{G_n} \left[I_{sc_n} + k_i (T - T_n) \right] \tag{13}$$

with G and G_n are the actual and nominal irradiance (STC conditions) [W/m²], respectively, I_{sc_n} is nominal short-circuit current, ki is coefficient of temperature effect on I_{sc_n} and T, T_n are the actual and nominal temperatures (STC conditions) [Kelvin], respectively.

Therefore, the expression for the output current of a PV cell I_{pv} can be written as follows:

$$I_{pv} = \frac{G}{G_n} \left[I_{sc,n} + k_i (T - T_n) \right] - I_0 \left[\exp \left[\frac{q(V_{pv} + R_s I)}{AkT} \right] - 1 \right] - \left[\frac{V_{pv} + R_s I}{R_{sh}} \right]$$
(14)

This study presents a PV system comprising two modules: Kyocera KD205GX-LP and SunPower SPR-305-WHT. Figure 4 (a) and (b) illustrate the I-V and P-V characteristics of each module, respectively. From the figures, it is evident that adjusting the terminal voltage of the PV module to Vmpp is essential to achieve the MPP. Under standard test conditions (STCs), the maximum extracted power reaches 100 kW for each PV module.

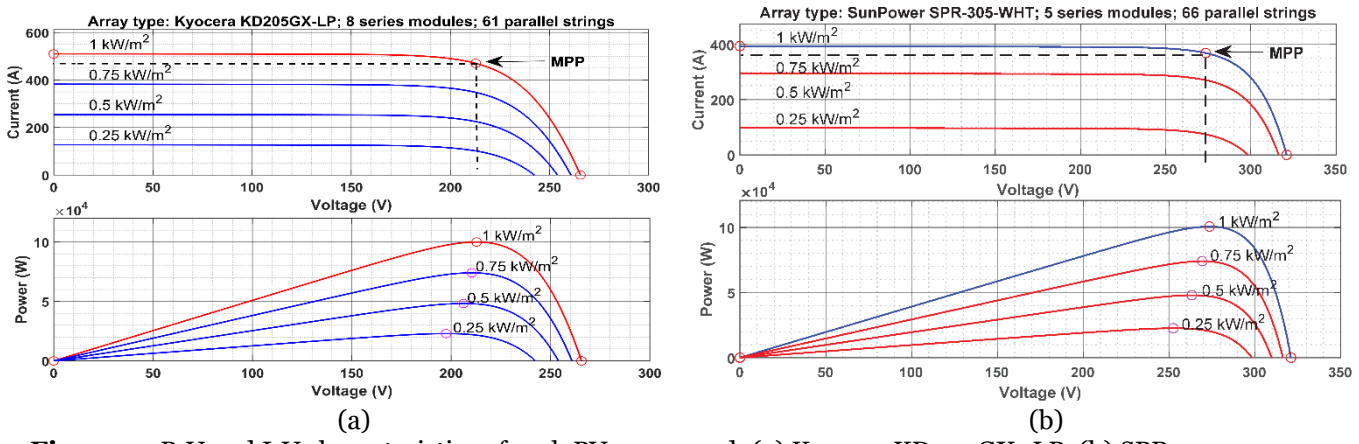


Figure 4: P-V and I-V characteristics of each PV array used: (a) Kyocera KD205GX-LP, (b) SPR-305-WHT.

C. MODELING OF AN HVDC-VSC SYSTEM

As shown in Figure 5, The VSC employs insulated gate bipolar transistors (IGBT) as switching elements for power conversion. Considering the ability of IGBTs to turn on and off via a gate signal, VSCs provide many benefits, like as insensitivity to AC grid power, providing black start capability in the system, as well as fast and discrete control of reactive and active bi-directional power flow, and it is capable of

2025, 10(4)

e-ISSN: 2468-4376

https://www.jisem-journal.com/

Research Article

operating independently in an isolated system. [14]. Furthermore, the power flow can be reversed by changing the DC direction without changing the DC voltage polarity.

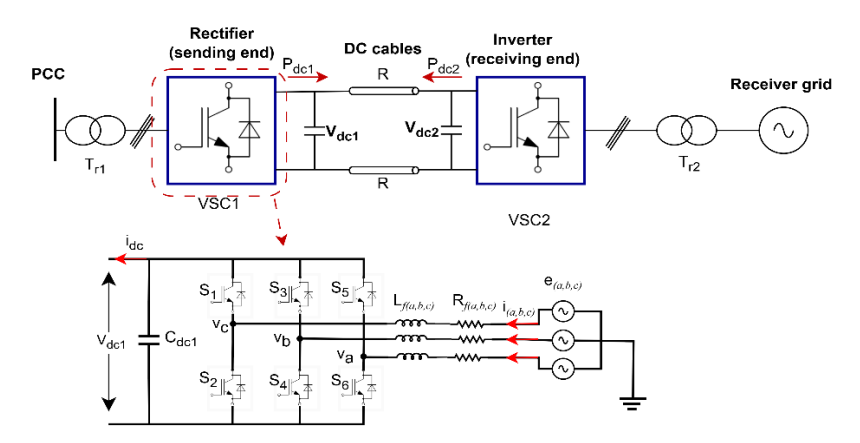


Figure 5: Design of basic VSC circuit.

Remark: In Figure 5, the rectifier and the inverter use voltage source converters (VSC), resulting in a symmetrical configuration of the VSC-HVDC system.

Mathematical modeling of the VSC-HVDC system involves dynamic equations that capture the behavior of the converter's AC side and the DC-link. The converter is modeled in a synchronous rotating reference frame (d-q frame) to simplify the analysis of three-phase AC quantities. By applying the Park transform for an AC side filter characterized by inductance L and resistance R, the dynamic equations for the converter voltage components v_d and v_q are given by the following [7]:

$$\begin{cases} v_d = -L\frac{d(i_d)}{dt} - Ri_d + \omega Li_q + e_d \\ v_q = -L\frac{d(i_q)}{dt} - Ri_q - \omega Li_d + e_q \end{cases} \tag{15}$$

where v_d and v_q are the output voltages of the converter on the d and q axes, respectively, e_d and e_q are the grid voltage, ω is the angular frequency of the synchronous reference frame, L and R are the filter inductance and resistance, respectively. The power balance between the AC input and the DC output is given by the following relationship:

$$\begin{cases} P = \frac{3}{2} (e_d i_d + e_q i_q) \\ Q = \frac{3}{2} (e_q i_d - e_d i_q) \end{cases}$$
 (16)

By aligning the grid voltage vector along the d-axis, a virtual grid flux vector can be assumed to lie along the q-axis. Under this reference frame, $e_q = 0$, and the instantaneous active and reactive power exchanged with the AC system can be expressed as:

$$\begin{cases} P = \frac{3}{2}e_d i_d \\ Q = -\frac{3}{2}e_d i_q \end{cases} \tag{17}$$

PROPOSED FFNN CONTROL TECHNIQUE

FFNN is a neural model inspired by the structure and behavior of neurons in the human brain, developed to handle nonlinear information and identify intricate patterns within data, a FFNN is formed of multiple layers of interconnected processing units, known as artificial neurons, data moves in one direction from the input layer via a hidden layer or more, and finally to the output layer without forming any feedback loops. Each layer is composed of neurons that perform a weighted summation of incoming signals, followed by the application of nonlinear activation functions. In a fully connected structure, each neuron in a given layer is linked to every neuron in the subsequent layer, enabling the

2025, 10(4)

e-ISSN: 2468-4376

https://www.jisem-journal.com/

Research Article

network to capture complex relationships within the data by iteratively adjusting the synaptic weights during the training process. [15].

The function of an FFNN lies in the supervised training process, where the network's weights are iteratively adjusted to minimize the discrepancy between the predicted and actual outputs. This discrepancy is quantified using error metrics such as mean squared error (MSE) or sum squared error (SSE) [16]. Optimization algorithms, such as the Levenberg–Marquardt algorithm are used during training to achieve fast convergence. After training, the FFNN's generalization ability is assessed through testing on unseen data. Figure 5 illustrates the steps involved in implementing the FFNN technique, while Figure 6 illustrates the structure of an FFNN.

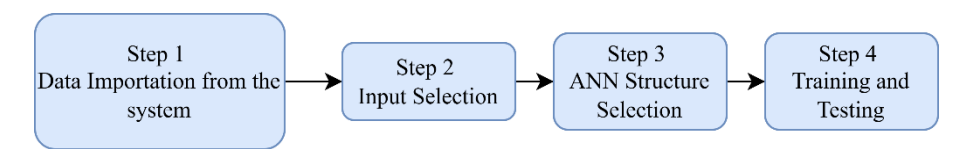


Figure 6: The steps of FFNN technique.

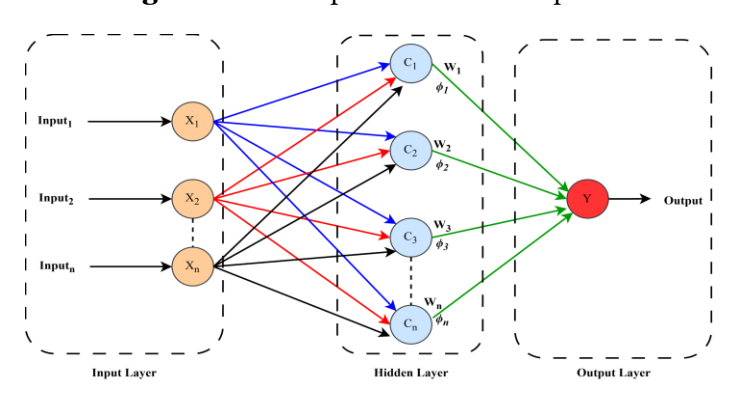


Figure 7: The structure of an FFNN.

The mean squared error is calculated using the following formula:

$$\begin{cases} MSE = \frac{1}{n} \sum_{i=1}^{n} (Y_{Ti} - Y_i)^2 \\ Y_i = f(\sum w_{ij} x_i + b) \end{cases}$$
 (17)

where n is the number of data points, Y_{Ti} is the actual (target) output and Y_i is the predicted output from the ANN, f(.) denotes the activation function, w_{ij} represents the connection weight, x_i is the input signal and b is the deviation value.

The FFNN is implemented in the following four main steps:

Step 1: data is imported from the simulation system; this data set must comprehensively capture the dynamic behavior of the system under various operating conditions to ensure network robustness. Step 2: the appropriate input variables are selected based on their effect on the system output and their importance to the control objectives. In our study, the inputs and outputs are determined according to the following approach:

$$\begin{cases} input_1 = e_{Vdc} = V_{dc}^* - V_{dc} \Rightarrow Ouput_1 = i_d^* \\ input_2 = e_Q = Q^* - Q_{meas} \Rightarrow Ouput_2 = i_q^* \\ input_3 = e_d = i_d^* - i_d \Rightarrow Ouput_3 = V_d^* \\ input_4 = e_q = i_q^* - i_q \Rightarrow Ouput_4 = V_q^* \end{cases}$$

2025, 10(4)

e-ISSN: 2468-4376

https://www.jisem-journal.com/

Research Article

Step 3: the structure of the FFNN is selected, including the number of hidden layers, the neurons per layer, and the activation functions.

Finally, in step 4, the network is trained using simulation-derived data. The Levenberg–Marquardt algorithm is employed to adjust the internal weights for optimal accuracy. Post-training, the model undergoes validation to confirm its ability to respond effectively under conditions not encountered during training.

SYSTEM CONTROL

A. PI CONTROL OF VSI SYSTEM

The grid-connected hybrid energy system is interfaced with the point of common coupling (PCC) via a three-phase, two-level voltage source inverter (VSI) employing pulse width modulation (PWM), thereby enabling efficient and high-quality power conversion. The VSI control structure adopts a dual-loop cascaded control strategy, consisting of an outer voltage regulation loop and an inner current control loop, both realized using PI controllers. The outer control loop is responsible for maintaining the DC-link voltage at a specified reference level, ensuring a stable power balance between the DC-side energy sources and the AC grid. While the inner current control loop regulates the injected grid currents i_d and i_q , which directly affect the active and reactive power exchanged with the grid. Figure 8 shows a classical PI control diagram in a VSI system.

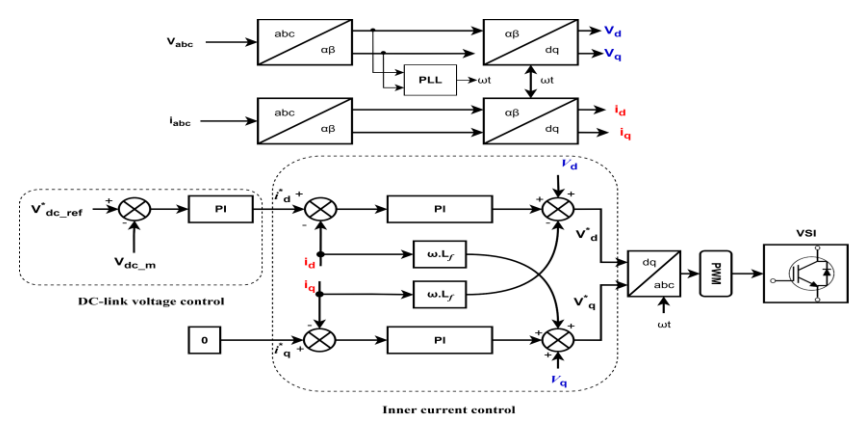


Figure 8: Classical PI control diagram of the VSI system.

B. VSC-HVDC CONTROL BASED ON PI-FFNN

The control of both VSC1 and VSC2 is implemented using a hierarchical dual-loop strategy composed of an inner current control loop and an outer loop. In VSC1, which manages the hybrid renewable energy source side, the inner loop regulates the grid-injected current in the synchronous rotating (d-q) reference frame, effectively decoupling the control of active and reactive power. Here, the database (inputs and outputs) is extracted through the PI controller and trained using the FFNN module, as shown in Figure 9.

The outer loop in this case governs the reference signals for active and reactive power based on system demands. Similarly, VSC2 located on the grid side, regulates the DC link voltage to maintain power balance between the two terminals. It also employs an outer loop to control the DC voltage and an inner current loop for fast dynamic response. Both VSCs utilize a similar current control structure, but the VSC2 connected to the grid has a phase-locked loop (PLL) to synchronize with the phase and frequency of the grid voltage [7]. The overall control configuration of VSC1 and VSC2 is illustrated in Figure 10, and Figure 11 also shows that DC-link voltage control and reactive power are controlled using the FFNN module.

e-ISSN: 2468-4376

https://www.jisem-journal.com/

Research Article

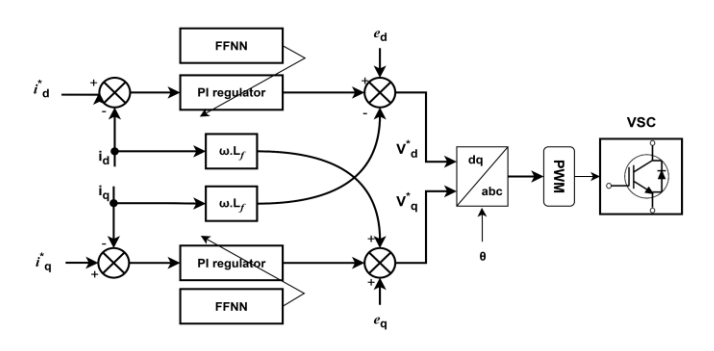


Figure 9: Inner control loop with FFNN.

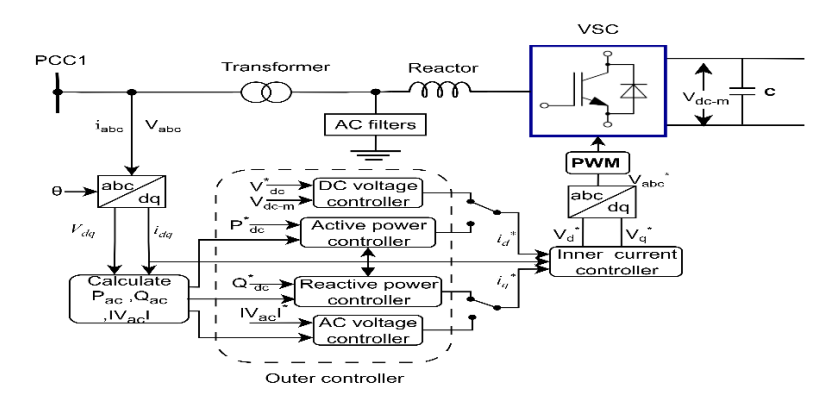


Figure 10: The overall control configuration.

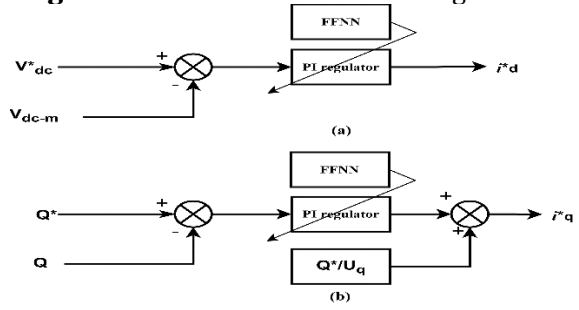


Figure 10: The outer controllers: (a) DC-link voltage control, (b) reactive power control.

SIMULATION RESULTS AND DISCUSSION

To validate the demonstrate the effectiveness of the proposed FFNN controller, a simulation of a hybrid renewable energy system consisting of two PV power stations and a wind power system integrated with a VSC-HVDC transmission link, was performed in a MATLAB/Simulink environment. The parameters of the system are provided in Table 1, while the specifications of the two PV modules in Table 2. All PI controller gains used in the system are shown in Table 3.

Table 1: The parameter values

System	Parameters Value		
	Utility grid voltage	50 KV	
	System frequency (f)	50 Hz	
Utility grid	Supply resistance	1.7857Ω	
	Supply inductance	0.0398 H	
	DC link capacitor of V _{dc}	0.048 F	
	Maximum wind power	100 KW	

2025, 10(4)

e-ISSN: 2468-4376

https://www.jisem-journal.com/

Research Article

	Stator phase resistance of PMSG (Rs)	0.0369 Ω
Wind system	Armature inductance of PMSG $L_d = L_q$	3.667×10 ⁻⁴ H
	Number of poles	4
	Leakage flux	0.253 Wb
	DC link Power	$3 \times 10^6 \text{ VA}$
HVDC-VSC	DC link voltage	3000 V
	DC link capacitor	0.068 F
	Line length	25 Km

Table 2: The specifications of PV modules

Parameters	KD205GX- LP	SPR-305- WHT	
Maximumi power (P_{mp})	100.7 KW	100.1 KW	
Maximumivoltage (V_{mp})	54.7 V	26.6 V	
Maximum current (I _{mp})	5.58 A	7.71 A	
Open-circuittvoltage (V_{oc})	64.2 V	33.2 A	
Short-circuittcurrent (I _{sc})	5.96 A	8.36 A	
Number of series cells Ns	5	8	
Number of parallel cells Np	66	61	

Table 3: Parameters of the PI gains

	Outer control loop		Inner loop	control
Gains	K _{i1}	K _{p1}	K _{i2}	K _{p2}
HRES	800	7	20	0.3
VSC1	275	2.5	8	0.1
VSC2	40	0.3	8	0.1

A. POWER INJECTION IN UTILITY GRID

Various climate scenarios were applied to hybrid energy sources, including fluctuating wind speeds and variable solar radiation, as shown in Figure 11.

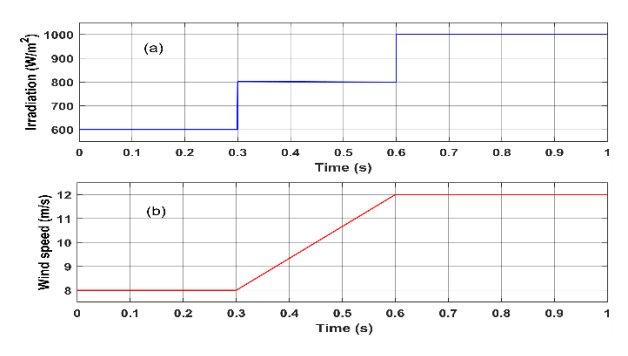


Figure 11: (a) Irradiation scenario; (b) wind speed scenario.

Figure 12 shows the power outputs generated by both the PV and wind energy systems, where the current is controlled by PI controllers. In addition, P&O-based MPPT was used to control the three boost converters for the PV and wind power systems, as shown in Figure 1. Figure 12 (a) presents the variation in the response speed of the power extracted from the PV stations when applying different irradiation values, while Figure 12 (b) shows the output power for the wind power system at varying wind speeds.

e-ISSN: 2468-4376

https://www.jisem-journal.com/

Research Article

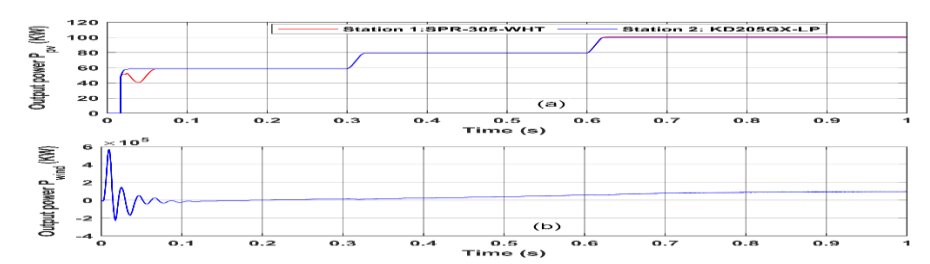


Figure 12: (a) PV power; (b) wind power.

One of the essential performance indicators for a HRES is the regulation of the DC link voltage. Figure 13 illustrates the dynamic response of the DC link voltage under varying climatic conditions. The results clearly show that the voltage consistently tracks its reference value, particularly during transient phases throughout the test period. This outcome demonstrates the system's capability to maintain a near-constant DC link voltage at 500 V, despite fluctuations in solar irradiance and wind speed, with only negligible voltage ripples observed.

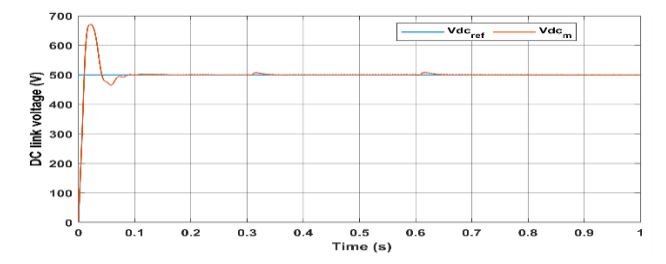


Figure 13: DC link voltage of HRES.

Figure 14 presents the instantaneous active and reactive power delivered by the utility grid. The power levels exhibit smooth variations both increases and decreases corresponding to the energy injected by the PV-wind hybrid system, with minimal oscillations observed throughout the operation.

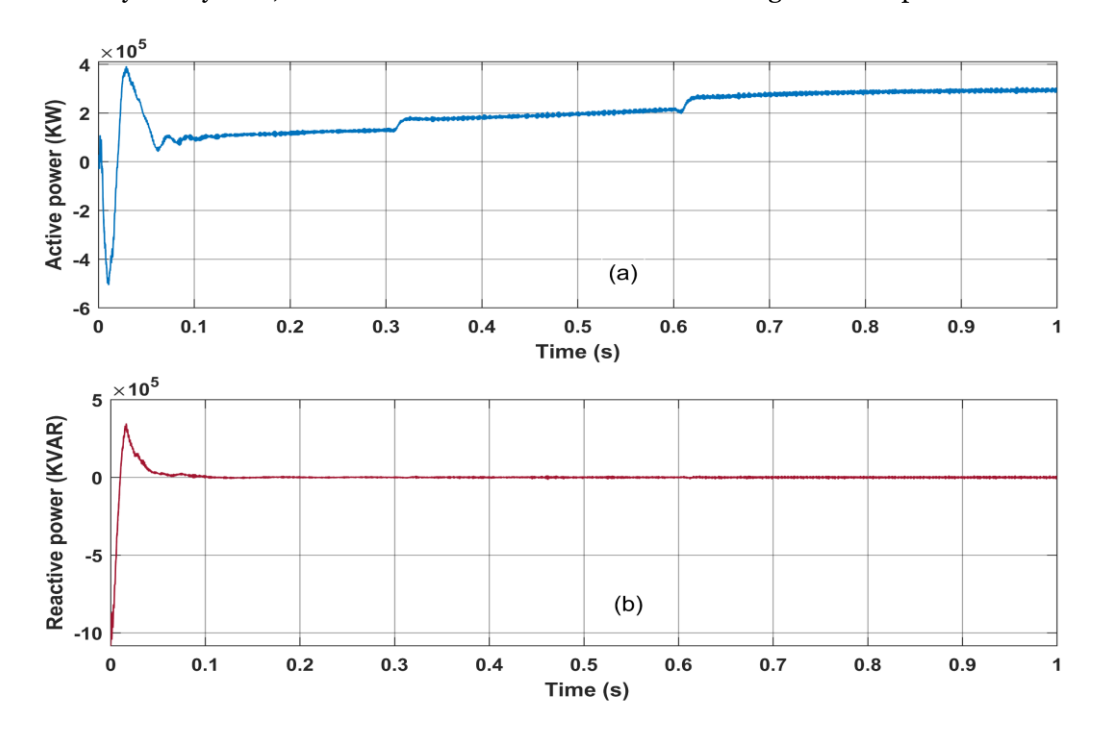


Figure 14: (a) instantaneous active power; (b) instantaneous reactive power.

e-ISSN: 2468-4376

https://www.jisem-journal.com/

Research Article

B. POWER INJECTION IN HVDC-VSC

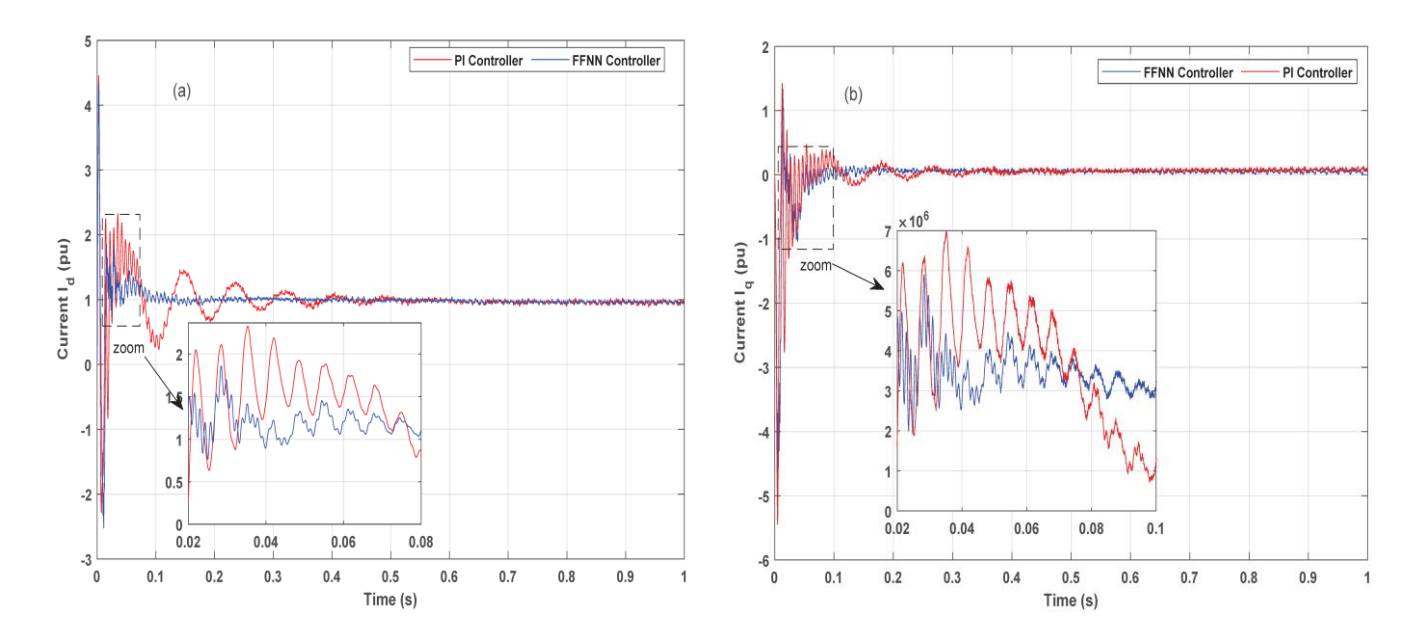


Figure 15: Current on the VSC 1 side: (a) i_d current and (b) i_q current.

Figure 15(a, b) presents a comparison of current controller responses i_d and i_q on the VSC 1 side, clearly showing the superior dynamic performance of the FFNN controller compared to the traditional PI controller in HRES integrated with HVDC-VSC. FFNN features a faster settling time, reduced overshoot, and significantly less fluctuation during transient periods. The FFNN controller provides smoother and more stable current regulation, effectively reducing high-frequency oscillations that persist under PI control. This improved performance can be attributed to the adaptive training of FFNN,as shown in Figure 16, which enables it to handle nonlinearity and system disturbances more efficiently than PI controllers.

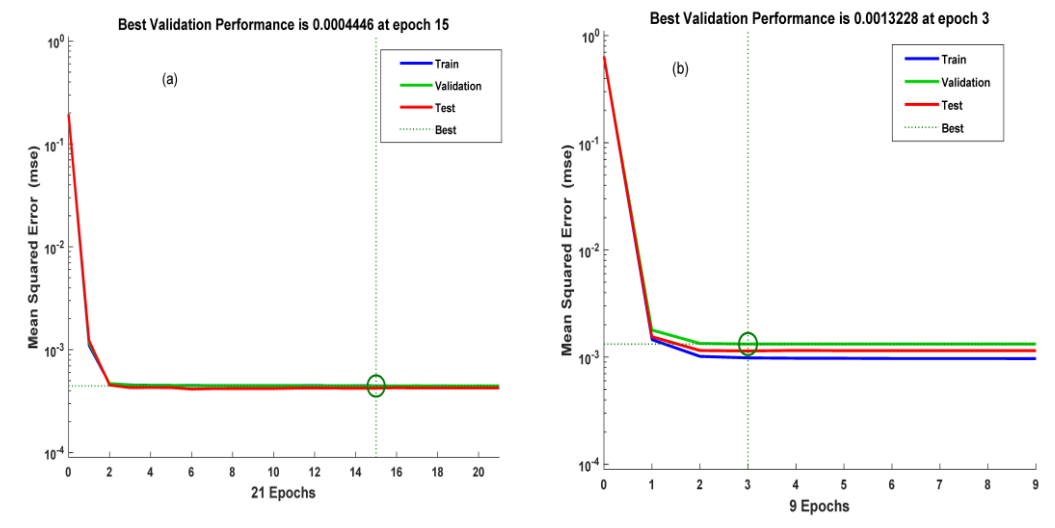


Figure 16: The training performance for current under FFNN control: (a) i_d current and (b) i_q current.

e-ISSN: 2468-4376

https://www.jisem-journal.com/

Research Article

Figure 17 (a) illustrates the DC link voltage (Vdc1) on the VSC1 side of the HVDC-VSC system and the improved control capability provided by the FFNN controller compared to a conventional PI controller. As shown in the figure, the FFNN controller achieves faster voltage regulation and exhibits significantly less oscillation during the transient phase. In contrast, the PI controller causes a noticeable overshoot and longer settling time, which can lead to unwanted stress on the transformer components. It is worth noting that the FFNN-controlled response follows the reference voltage (3000 V) more accurately, with minimal steady-state error, maintaining stability even under rapid dynamic changes. Figure 17 (b) shows the training performance for Vdc under FFNN control.

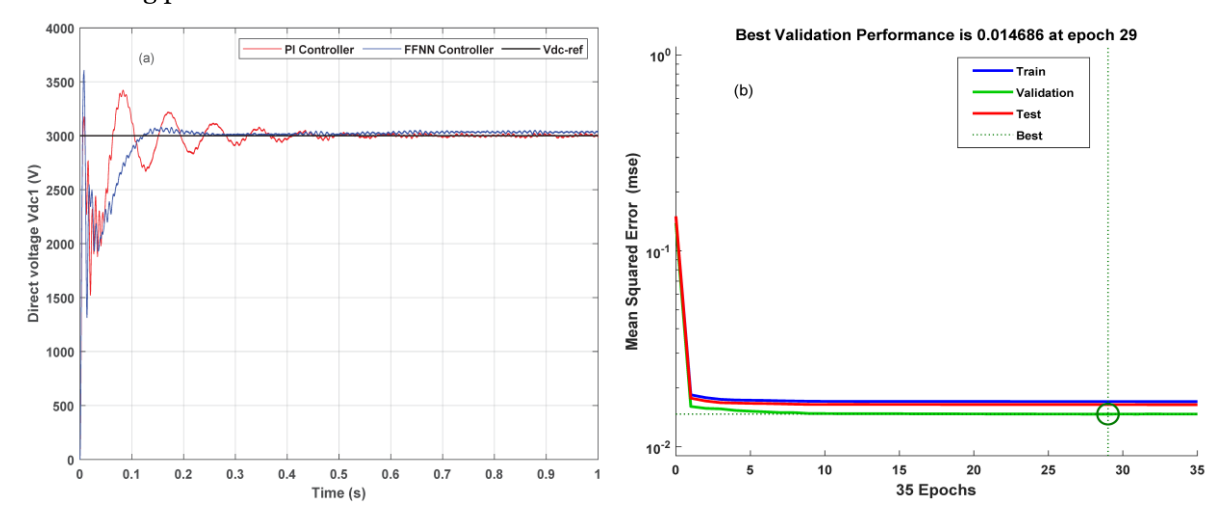


Figure 16: (a) The DC-link voltage on the VSC 1 side, (b) The training performance for Vdc current under FFNN control.

Figure 17 illustrates the active and reactive power in VSC1, respectively. while Figure 18 illustrates the active and reactive power in VSC2, respectively. The FFNN controller shows superior dynamic performance compared to the PI controller. It is worth noting that FFNN shows faster attenuation of oscillations and reduction of overshoot during transient conditions. For VSC1, it is clear that FFNN produces lower peak deviations and stabilizes faster than the PI controller. Similarly, for VSC2, the FFNN controller effectively mitigates high-frequency oscillations and achieves more stable power exchange shortly thereafter. Figure 19 shows the training performance for reactive power under FFNN control.

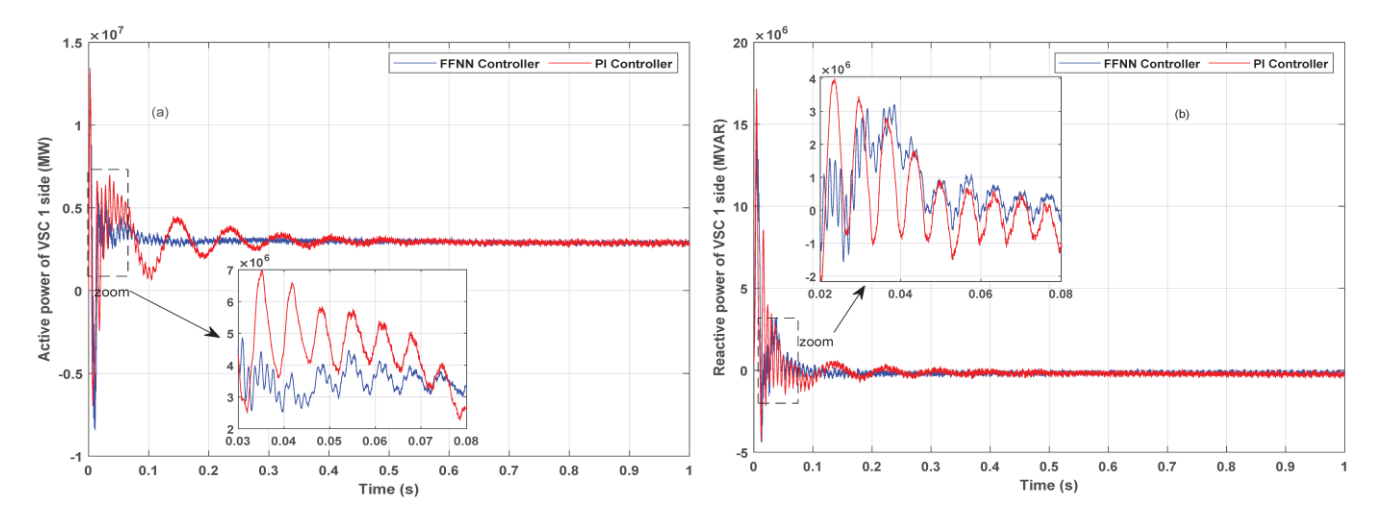


Figure 17: (a) Instantaneous active power on the VSC 1 side, (b) instantaneous reactive power on the VSC 1 side.

e-ISSN: 2468-4376

https://www.jisem-journal.com/

Research Article

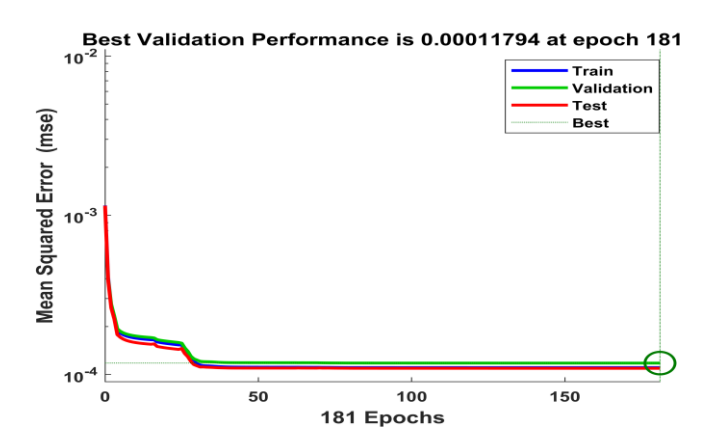


Figure 18: (a) Instantaneous active power on the VSC 2 side, (b) instantaneous reactive power on the VSC 2 side.

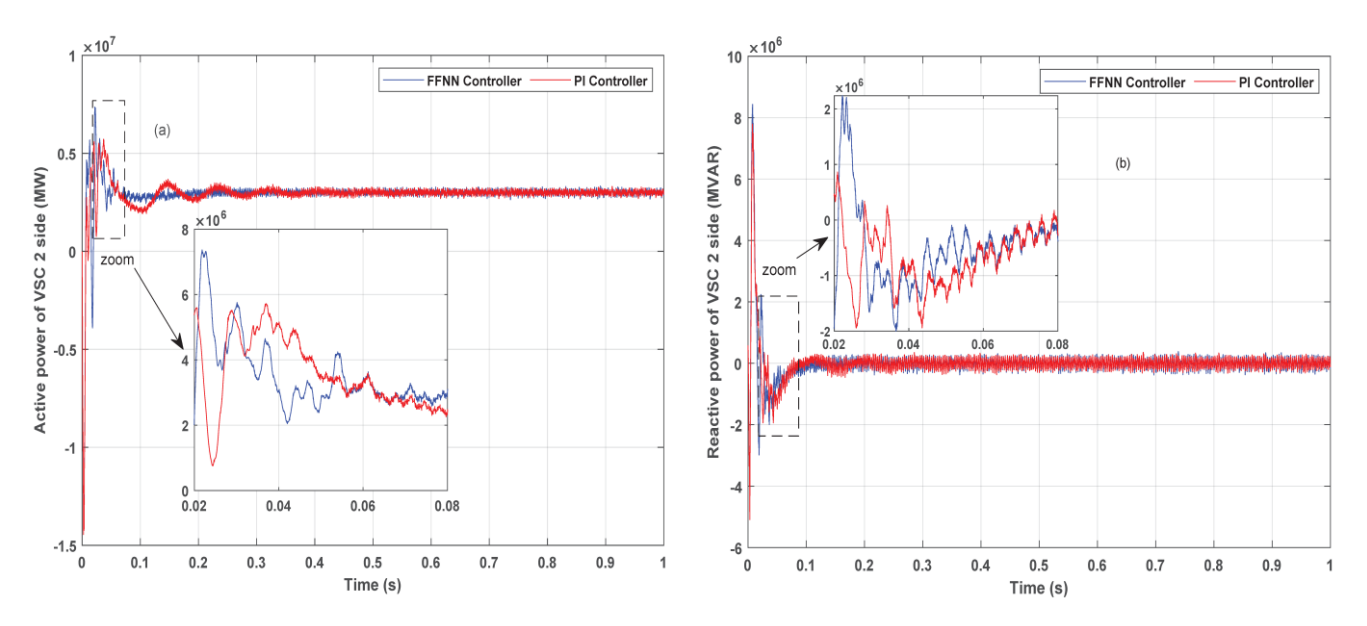


Figure 19: The training performance for reactive power under FFNN control.

CONCLUSION

This paper presented a comparison of PI and FFNN controllers for current and power regulation in an HVDC-VSC integrated hybrid renewable energy system. Simulation results confirmed that the FFNN controller outperforms the conventional PI controller in both transient and steady-state responses. It demonstrated superior performance in regulating d-axis and q-axis currents, achieving reduced overshoot, faster settling time, and improved damping. In addition, the FFNN ensured more accurate and stable DC-link voltage control, minimizing oscillations, and tracking errors. Enhanced active and reactive power regulation at both converter terminals further highlighted the FFNN's ability to handle nonlinearities and system disturbances effectively. Overall, the FFNN controller offers a robust and high-performance alternative for intelligent control in modern HVDC-connected renewable systems.

2025, 10(4)

e-ISSN: 2468-4376

https://www.jisem-journal.com/

Research Article

Future work will focus on validating the results in hardware-in-the-loop (HIL) systems to assess their practicality in real-time.

REFRENCES

- [1] S. Asiaban et al., "Wind and Solar Intermittency and the Associated Integration Challenges: A Comprehensive Review Including the Status in the Belgian Power System," Energies, vol. 14, no. 9, p. 2630, Jan. 2021, doi: https://doi.org/10.3390/en14092630.
- [2] Q. Hassan, S. Algburi, A. Z. Sameen, H. M. Salman, and M. Jaszczur, "A Review of Hybrid Renewable Energy systems: Solar and wind-powered solutions: Challenges, opportunities, and Policy Implications," Results in Engineering, vol. 20, no. 1, p. 101621, Nov. 2023, doi: https://doi.org/10.1016/j.rineng.2023.101621.
- [3] N. Samala and C. Bethi, "Harnessing synergy: a holistic review of hybrid renewable energy systems and unified power quality conditioner integration," Journal of Electrical Systems and Information Technology, vol. 12, no. 1, Feb. 2025, doi: https://doi.org/10.1186/s43067-025-00193-1.
- [4] R. Zeng and Y. Wang, "Improved Frequency Control Strategy for Offshore Wind Farm Integration via VSC-HVDC," Energies, vol. 15, no. 17, p. 6363, Aug. 2022, doi: https://doi.org/10.3390/en15176363.
- [5] D. Kumar, Wajiha Shireen, and N. Ram, "Grid Integration of Offshore Wind Energy: A Review on Fault Ride Through Techniques for MMC-HVDC Systems," Energies, vol. 17, no. 21, pp. 5308–5308, Oct. 2024, doi: https://doi.org/10.3390/en17215308.
- [6] C. H. Lin, "The Impact of Integration of the VSC-HVDC Connected Offshore Wind Farm on Torsional Vibrations of Steam Turbine Generators," Sustainability, vol. 15, no. 1, p. 197, Dec. 2022, doi: https://doi.org/10.3390/su15010197.
- [7] L. Mazouz, S. A. Zidi, M. Khatir, T. Benmessaoud, and S. Saadi, "Particle swarm optimization-based PI controller of VSC-HVDC system connected to a wind farm," International Journal of System Assurance Engineering and Management, vol. 7, no. S1, pp. 239–246, Sep. 2015, doi: https://doi.org/10.1007/s13198-015-0375-1.
- [8] Roheen Qamar and Baqar Ali Zardari , Trans., "Artificial Neural Networks: An Overview", Mesopotamian Journal of Computer Science, vol. 2023, pp. 124–133, Aug. 2023, doi: https://doi.org/10.58496/mjcsc/2023/015.
- [9] A. Mahdjoubi, lazreg taibaoui, and B. Zegnini, "Optimizing Artificial Neural Networks with Particle Swarm Optimization for Accurate Prediction of Insulator Flashover Voltage Under Dry and Rainy Conditions," ITEGAM- Journal of Engineering and Technology for Industrial Applications (ITEGAM-JETIA, vol. 11, no. 51, 2025, doi: https://doi.org/10.5935/jetia.v11i51.1467.
- [10] R. S. Jawad and H. Abid, "Fault Detection in HVDC System with Gray Wolf Optimization Algorithm Based on Artificial Neural Network," Energies, vol. 15, no. 20, p. 7775, Oct. 2022, doi: https://doi.org/10.3390/en15207775.
- [11] Btissam Majout et al., "Improvement of PMSG-Based Wind Energy Conversion System Using Developed Sliding Mode Control," Energies, vol. 15, no. 5, pp. 1625–1625, Feb. 2022, doi: https://doi.org/10.3390/en15051625.
- [12] H.-W. Kim, S.-S. Kim, and H.-S. Ko, "Modeling and control of PMSG-based variable-speed wind turbine," Electric Power Systems Research, vol. 80, no. 1, pp. 46–52, Jan. 2010, doi: https://doi.org/10.1016/j.epsr.2009.08.003.
- [13] K. Cherif, Mazouz Lakhdar, Kouzou Abdellah, E. Ahmed, and Karboua Djaloul, "Fuzzy Logic Controller based Maximum Power Point Tracking Using DC/DC Boost Converter for PV System," 2022 19th International Multi-Conference on Systems, Signals & Devices (SSD), pp. 1992–1997, May 2022, doi: https://doi.org/10.1109/ssd54932.2022.9955835.

2025, 10(4)

e-ISSN: 2468-4376

https://www.jisem-journal.com/

Research Article

- [14] S. Song, S. Hwang, B. Ko, S. Cha, and G. Jang, "Novel Transient Power Control Schemes for BTB VSCs to Improve Angle Stability," Applied Sciences, vol. 8, no. 8, p. 1350, Aug. 2018, doi: https://doi.org/10.3390/app8081350.
- [15] E. Viera-Martin, J. F. Gómez-Aguilar, J. E. Solís-Pérez, José Alfredo Hernández-Pérez, and R.F. Escobar-Jiménez, "Artificial neural networks: a practical review of applications involving fractional calculus," European Physical Journal-special Topics, vol. 231, no. 10, pp. 2059–2095, Feb. 2022, doi: https://doi.org/10.1140/epjs/s11734-022-00455-3.
- [16] Cherif Kellal, Mazouz Lakhdar, Abdellah Kouzou, and Abdelkdaer Ouacel, "An ANN-based Maximum Power Point Tracking Using DC/DC Boost Converter for PV System," pp. 1–6, May 2023, doi: https://doi.org/10.1109/icrsetoset56772.2023.10525465.